Stochastic Interference Modeling and Experimental Validation for Pulse-Based Terahertz Communication

Zahed Hossain, *Member, IEEE*, Carley N. Mollica, John F. Federici, and Josep Miquel Jornet, *Member, IEEE*

***Abstract*— The transmission of one-hundred-femtosecond-long pulses by following an ON-OFF keying modulation spread in time has been proposed as a way to enable Terahertz (THz)-band (0.1–10 THz) communications over short distances. Such modulation minimizes the probability of collisions due to the very small time that the channel is occupied by a user. However, given that many of the envisioned applications involve very large node densities, multi-user interference becomes unavoidable. In this paper, a stochastic model of multi-user interference is developed and experimentally validated. The model takes into account the fact that the interference power at the receiver is not a combination of the received powers from the individual nodes, but the power of the combination of the received signal amplitudes. For this, first, a mathematical framework is developed to compute the probability density function (PDF) of the interference generated by one interfering node at the receiver, starting from the PDFs of the pulse received energy and the PDF of the pulse shape. Then, the model is extended to account for multiple nodes which can constructively or destructively interfere. The developed model is experimentally validated by means of an innovative setup and the extensive numerical results are provided to analyze the trends of multi-user interference in pulse-based THz communications.**

***Index Terms*— Terahertz communications, multiple access interference, pulse modulation, experimental characterization, stochastic processes.**

I. Introduction

OVER the last decade, wireless data traffic has experienced an explosive growth due to a change in the way today's society creates, shares and consumes information. This change has been accompanied by an increasing demand for higher speed wireless communication anywhere, anytime. To satisfy this demand, wireless data rates has been improved much faster than wired counterpart and will continue to do so for a while [4]. Following this trend, wireless multi-Gigabit-per-second (Gbps) and Terabit-per-second (Tbps) links are expected to become a reality within the next five to ten years [1]. It is not possible to achieve Tbps link with the existing spectrum band in use due to prohibitively high spectral efficiency required. Even with the 7GHz continuous bandwidth available in the millimeter wave systems, an spectral efficiency of over 100 bits/second/Hz is required to achieve Tbps which is very difficult. In this context, Terahertz (THz)-band (0.1-10 THz) communication [1], [6], [7], [21] is envisioned as a key technology to satisfy the need for such very high data-rates, both in traditional networking paradigms as well as in novel nanoscale machine communication networks.

For many years, the lack of compact and efficient ways to generate and detect THz-band signals has limited the feasibility of such communication systems. However, within the last five years, outstanding progress has been achieved towards the development of compact THz-band transceivers and antennas. Different technologies have been considered to date, ranging from Silicon Germanium and compound semiconductor technologies based on III-V materials [20], [29], to photonic devices such as Quantum Cascade Lasers [22], [23], [30], [33] and, more recently, the use of nanomaterials such as graphene is enabling the development of novel plasmonic transceivers and antennas, which intrinsically operate in the THz-band [8], [16], [18], [24].

The THz band provides wireless communication devices with an unprecedentedly large bandwidth, ranging from several tens of GHz up to a few THz [15], [28]. In addition to the very high spreading loss at this high frequency, the main phenomenon affecting the propagation of THz-band signals is the absorption by water vapor molecules. For communication distances below 1 m, where the number of molecules found along the path is small, the THz band behaves as a single transmission window several THz wide. This very wide bandwidth motivates the use of pulse based modulation scheme for short range communications similar to Impulse Radio Ultra-Wide-Band (IR-UWB) [25]. For distances beyond a few meters, molecular absorption defines multiple transmission windows, tens to hundreds of GHz wide each. In this case, the carrier based modulation is more suitable and highly directional antennas are needed to overcome the severe path loss. In this paper we focus on the short range THz communication.

For short-range THz communications (i.e., distances up to a few meters), the transmission of one-hundred-femtosecond-long pulses by following an on-off keying modulation spread in time has been recently proposed [17]. The power spectral density (PSD) of such pulses, which can be generated

Manuscript received September 17, 2018; revised January 27, 2019 and May 12, 2019; accepted May 22, 2019. Date of publication June 12, 2019; date of current version August 12, 2019. This work was supported in part by U.S. National Science Foundation (NSF) under Grant CNS-1730148 and Grant CNS-1846268. This paper was presented at the Proceedings of the ACM NanoCom'16 [13]. The associate editor coordinating the review of this paper and approving it for publication was K. Haneda. *(Corresponding author: Zahed Hossain.)*

Z. Hossain was with the University at Buffalo, The State University of New York, Buffalo, NY 14260 USA. He is now with Intel Corporation (e-mail: zahedhos@buffalo.edu).

C. N. Mollica and J. F. Federici are with the Department of Physics, New Jersey Institute of Technology, Newark, NJ 07102 USA.

J. M. Jornet is with the Department of Electrical Engineering, University at Buffalo, The State University of New York, Buffalo, NY 14260 USA.

Color versions of one or more of the figures in this paper are available online at http://ieeexplore.ieee.org.

Digital Object Identifier 10.1109/TWC.2019.2920965

1536-1276 © 2019 IEEE. Personal use is permitted, but republication/redistribution requires IEEE permission.
See http://www.ieee.org/publications_standards/publications/rights/index.html for more information.

and detected by means of different electronic, photonic and plasmonic devices, has its main frequency components under 4 THz. By utilizing an on-off keying modulation, the transmitter can reduce its energy consumption by remaining silent during the transmission of logical "0s", and by spreading the transmission of the pulses in time, concurrent transmissions can be multiplexed in time.

The transmission of ultra-short pulses minimizes the probability of collisions due to the very small time that the channel is occupied by each user. However, given that many of the envisioned applications of THz-band communications involve very large node densities (e.g., wireless nanosensor networks or networks on chip), multi-user interference results unavoidably. Commercially available terahertz signal consists of hundred femtosecond long gaussian pulses with a peak power of around 10 μW [6]. As a result, the transmitted signals have large fluctuations between positive and negative amplitude values. The existing works, summarized in Sec. II, in multiuser interference modeling consider received signal power instead of the received signal amplitude, and hence ignore the fact that the interference can be constructive or destructive. This can cause unrealistically large values of interference due to the high amplitude of the pulses.

In this paper, we develop a stochastic model of multi-user interference in pulse-based THz-band communications and experimentally validate it. This model is developed by considering the fact that the interference power at the receiver is not a combination of the received powers from the individual nodes, rather the power of the combination of the signal amplitudes. For this, first, we obtain the probability density function (PDF) of the interference generated by one interfering node at the receiver, starting from the PDFs of the pulse received energy and the PDF of the pulse shape. Then, we extend this model to account for multiple nodes which can constructively or destructively interfere. Finally, we validate the model by comparing the results with experimental measurements.

The main contributions of this paper are threefold. Using the tools of stochastic geometry we

- analytically model the PDF of interference considering shape of the transmitted signal.
- show that the interference distribution is not Gaussian for low density networks, however it converges to Gaussian as the number of nodes become much greater than ratio of symbol duration to pulse duration
- validate the analytical model by experimental results for 20 nodes using a novel interference generating setup.

The rest of the paper is organized as follows. In Sec. II, we describe the related works. Sec. III-A, describes the system model regarding THz channel characteristics, network topology and signaling scheme. The stochastic model of multi-user interference is developed in Sec. IV. We describe our experimental setup, validate the analytical model and provide numerical results in Sec. V. Finally, we conclude the paper in Section VI.

II. Related Works

Stochastic geometry has been used extensively to model and analyze random wireless networks [2], [3], [10], [34]. These models assume infinite number of nodes in an infinite area for analytical tractability. Analysis of wireless networks with finite area and finite number of nodes has been performed for millimiter wave communications in [32]. These models can not be directly used in THz band networks as they do not take into account the peculiarities of the THz band channel, such as the exponential attenuation caused by the molecular absorption loss. Reference [9], [31] have shown that, the blockage of signal by obstacles can cause significant loss in signal strength for millimeter wave communication networks. THz band is even higher in frequency and experiences more blockage by obstacles. However, as mentioned in [19], the blocking can be modeled as a blocking probability in the stochastic models and thus as a thinning process. More Recently, there have been several works on stochastic interference modeling for THz band communication networks that take into account the molecular absorption loss [19], [26], [35]. All of the previously mentioned works compute total interference by adding the received powers from individual nodes. However, the interference happens in the amplitude of the received signal, i.e., interference is the sum of the electric fields from individual nodes. Hence, modeling the interference as addition of fields can provide more accurate interference power distribution than when it is modeled as sum of powers from individual nodes [5], [13]. In addition, these models were built considering the macroscale operation of THz band where carrier based waveforms are utilized. In [5], the authors have considered the baseband processing of carrier-wave based signals where the effect of pulse shape on the inter-ference may not be important as long as sampling is done at the right moment. However, in pulse-based THz communication where the pulses are hundreds of femtoseconds long and tens of pico-seconds apart, sampling at the right moment is almost impossible. As a result, energy detection based receivers are used and pulse shape plays important role in calculating the aggregate interference. Some recent interference models have been developed for pulse-based THz band communication networks [14], [17]. However, these models do not take into account the specific waveforms that are being transmitted (e.g., Gaussian-shaped pulses).

III. System Model

In this section, we describe the system model utilized in the paper. To model the multi-user interference, we first need to take into account THz signal propagation, the spatial distribution of the nodes as well as their temporal activity.

A. THz Signal Propagation

The propagation of electromagnetic waves at THz-band frequencies is mainly determined by the spreading loss and the molecular absorption loss. In particular, based on the THz-band channel model introduced in [15], the signal power at a distance d from the transmitter, P_r is

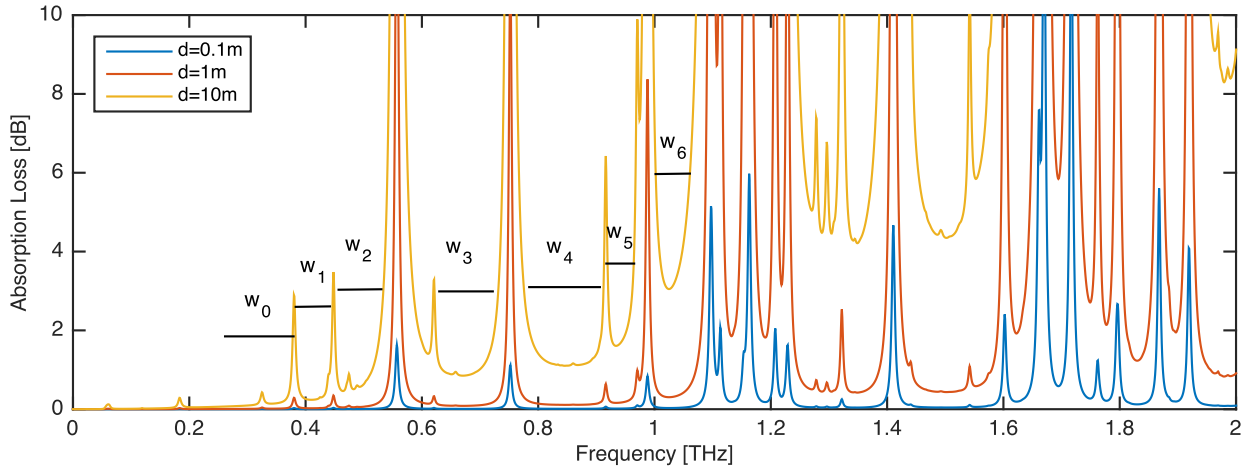

Fig. 1. Molecular absorption loss A_{abs} in dB at different transmission distances.

given by

$$P_r(d) = \int_{B(d)} S_t(f) \left|H_c(f,d)\right|^2 \left|H_r(f)\right|^2 df, \quad (1)$$

where S_t is the power spectral density (p.s.d) of the transmitted signal, B stands for the bandwidth and f refers to frequency. H_r in (1) refers to the receiver frequency response, which we consider an ideal low-pass filter with bandwidth B, for the time being. H_c refers to the THz-band channel frequency response, which is given by

$$H_c(f,d) = \left(\frac{c}{4\pi f d}\right) \exp\left(-\frac{k_{abs}(f)\, d}{2} - i2\pi f \frac{d}{c}\right), \quad (2)$$

where c refers to the speed of light and k_{abs} is the molecular absorption coefficient of the medium. This parameter depends on the molecular composition of the transmission medium, i.e., the type and concentration of molecules found in the channel and is given by [15].

In Figure 1, the molecular absorption loss in dB is shown for different transmission distances and in the frequency range between 0.1–2 THz, for a standard atmosphere with 40% humidity. There are several observations to be made. First and foremost, molecular absorption plays a key role in defining the available transmission bandwidth. For distances below one meter, the THz band behaves as a single transmission window several THz wide. However, for longer distances, the absorption from water vapor defines multiple transmission windows. Second, it is clear from Figure 1 that absorption at THz frequencies is much more dominant than at mm-wave bands. For example, at the 60 GHz peak, the absorption is approximately 12 dB/km, whereas at THz frequencies, the absorption peaks are easily above 10 dB at distances around 10 meters.

As shown in [14], for the distances considered in our analysis, between a few hundred of micrometers and up to one meter, received signal power P_r can be approximated as a function of the distance d by the polynomial

$$P_r(d) = \beta d^{-\alpha}, \quad (3)$$

where α and β are two constants which depend on the specific channel molecular composition as well as on the power and the shape of the transmitted signal. In this paper, we consider the amplitude of the interference instead of power. The amplitude of a signal is the square root of the signal energy which can be found by integrating the signal power over the signal duration. From the measured data in our experiment, the received signal energy can also be approximated as a function of distance d by the following polynomial

$$e_p(d) = \xi d^{-\eta}, \quad (4)$$

where ξ and η are two constants which depend on the specific channel molecular composition as well as on the energy and the shape of the transmitted signal.

B. Network Topology

We consider that nodes are randomly distributed in space by following a spatial Poisson process with rate λ. Without loss of generality, we consider that the intended receiver is located at the center of a disc of radius a and area $A = \pi a^2$. The probability of finding k nodes in the disc is given by

$$P(k \in A) = \frac{(\lambda \pi a^2)^k}{k!} e^{-\lambda \pi a^2}. \quad (5)$$

Under the Poisson assumption, the locations of the nodes follow independent and identically distributed uniform distributions. If d is the distance to the origin from a point that is uniformly distributed in A, then the PDF of the distance distribution D is given by

$$f_D(d) = \begin{cases} \dfrac{2d}{a^2} & \text{for } 0 < d < a \\ 0 & \text{otherwise.} \end{cases} \quad (6)$$

However, there is a minimum distance between the receiver and unintended transmitters as shown in Figure 2. This is usually the case, as the interfering node and the receiver node can not be at the same location [27]. Lets denote the minimum

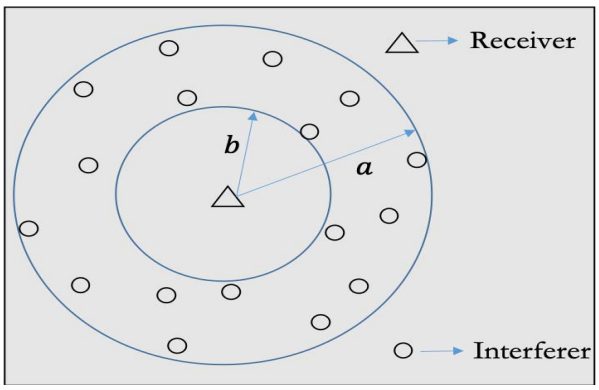

Fig. 2. Illustration of network topology.

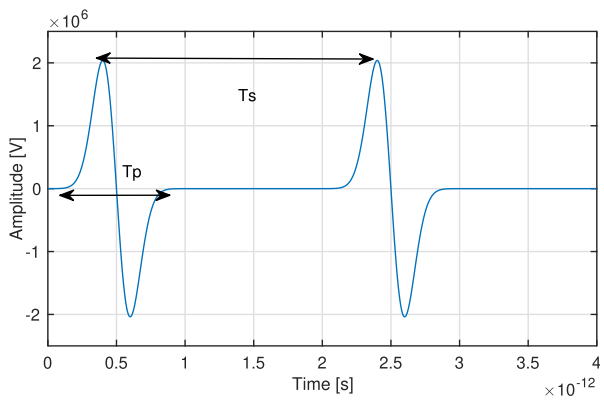

Fig. 3. Illustration of a TS-OOK transmission.

distance of interferers from the receiver as b. Then the the distribution of the distance is given as following

$$f_D(d) = \begin{cases} \dfrac{2d}{a^2 - b^2} & \text{for } b < d < a \\ 0 & \text{otherwise.} \end{cases} \tag{7}$$

C. Physical and Link Layers

We consider that nodes communicate by utilizing TS-OOK [17]. In this scheme, a symbol "1" is sent by transmitting a hundred-femtosecond long pulse and a symbol "0" is sent by silence, i.e., a node does not transmit anything (Figure 3). The time between symbols T_s is much longer than the symbol duration T_p, i.e., $\beta = T_s/T_p \gg 1$.

The pulses in TS-OOK are usually modeled as Gaussian-shaped. More specifically, the radiated pulses $s(t)$ resemble the first time derivative of a Gaussian pulse,

$$s(t) = \frac{dx(t)}{dt} = -\frac{(t-\mu)}{\sigma^2} x(t), \text{ with} \tag{8}$$

$$x(t) = a_0 \frac{e^{-\frac{(t-\mu)^2}{2\sigma^2}}}{\sqrt{2\pi}\sigma}, \tag{9}$$

where a_0 is a normalizing constant to adjust the pulse total energy, σ is the standard deviation of the Gaussian pulse in seconds, and μ is the center of the pulse in time, given in seconds. The total length of the radiated pulses $s(t)$ is approximately $T_p = 7\sigma$.

TS-OOK enables robust and concurrent communication among nodes. In the envisioned scenarios, nodes can start transmitting at any time without being synchronized or controlled by any type of network central entity. However, due to the fact that the time between transmissions T_s is much longer than the pulse duration T_p, several nodes can concurrently use the channel without necessarily affecting each other. In addition, the very short symbol duration T_p makes collisions between symbols highly unlikely. However, as the number of communicating nodes increases, interference becomes a problem, as we show in the next section.

A collision between symbols will occur when two or more symbols overlap at the receiver. In TS-OOK, by considering also a Poisson distribution of the arrival of pulses in time, the probability of having an arrival during symbol duration T_s follows a uniform distribution with PDF given below,

$$f_{T_s}(t) = \begin{cases} \dfrac{1}{T_s} & \text{for } 0 < t < T_s \\ 0 & \text{otherwise.} \end{cases} \tag{10}$$

IV. Interference Model

In the existing interference models, the total interference power at the receiver is obtained as the addition of the interference power from each node. However, by considering the received signal power instead of the received signal amplitude, the fact that interference can be either constructive or destructive is effectively neglected. Hence, summing the powers can result in unrealistically large values of interference, specially when the transmitted signals have large fluctuations between positive and negative amplitude values. Maxwell's equations are linear equations and, thus, the signals transmitted by different users are added in the channel, always. According to their relative phase, they might experience constructive or destructive interference, leading to fading. We agree that, in traditional carrier-based communication systems, in which the modulated information is in the amplitude, phase and frequency of the signal, the accurate modeling of interference starting from the addition of amplitudes is very challenging and, thus, the emphasis has been on the modeling of interference starting from the power. However, in the system under analysis in this paper, we consider that nodes communicate by utilizing a pulse-based modulation scheme. Every transmitted signal consists of pulses (logical "1"s) and silences (logical "0"s). All the signals look effectively the same, the only difference is in the sequence between "0"s and "1"s. This system, which might appear as a simplification of reality, is not far from what is already being utilized for THz sensing and spectroscopy, and, thus, it has a practical motiva-tion. For this system, we can estimate the real interference, starting from the amplitude, because of the shape of the signals, without any further assumption. From amplitude, we can then also obtain the distribution of the interference energy or power. We taylor our model to Gaussian-shaped pulses, but the same methodology could be utilized for any other waveform.

In order to characterize the interference, we observe the signals at the receiver. For the system model described in

Section III-A, the signal $y(t)$ at the receiver can be written as

$$y(t) = \sum_{u=1}^{U} \left(s(t-\tau_u)\right) * h(t, d_u) + n(t), \tag{11}$$

where U is the total number of nodes in the network, $s(t-\tau_u)$ is the transmitted signal along with the delay τ_u, $h(t, d_u)$ is the system impulse response, $*$ denotes convolution, and $n(t)$ is the noise at the receiver. The system impulse response $h(t, d_u)$ captures the impact of the THz-band channel, and is obtained as in [17].

If we consider the signal from user $u = 1$ as the intended signal, the total interference is given by

$$i(t) = \sum_{u=2}^{U} i_u(t), \tag{12}$$

where $i_u(t)$ is the interference at receiver due to each node u. By focusing on one specific symbol, without losing generality, $i_u(t)$ can be written as

$$i_u(t) = \sqrt{e_{p,u}} p\left(t - \tau_{t,u}\right), \tag{13}$$

where $e_{p,u}$ stands for the energy of the received pulse, $p(t)$ is the shape of the pulse with unitary energy, and $\tau_{t,u}$ refers to the total delay (initial delay and propagation delay).

Given that nodes are randomly distributed in space and uncoordinatedly transmitting in time, the PDF of the interference distribution I_u generated by a node u can be modeled as a function of two random variables, namely, the energy e_p of the pulse, with corresponding random variable E_p, and the shape $p(t)$ of the pulse, with corresponding random variable P.

As illustrated in (4), the energy of the received pulse depends on the transmitted pulse energy, which we consider a parameter in our analysis, and the distance between the nodes, which is a random variable D with PDF given by (7). Therefore, the PDF of E_p can be derived from the PDF of D as follows:

$$f_{E_p} = \frac{f_D(f^{-1}(e_p))}{f'(f^{-1}(e_p))}, \tag{14}$$

where f^{-1} denotes the inverse and f' denotes the first derivative of e_p. The PDF of E_p can only be analytically obtained if $e_p(d)$ is invertible. By computing the inverse function of (4), and combining it with (7) in (14), we obtain

$$f_{E_p}(e_p) = \begin{cases} \dfrac{2\xi^{\frac{2}{\eta}}}{(a^2-b^2)\eta} e_p^{-\frac{2+\eta}{\eta}} & \text{for } \xi a^{-\eta} < e_p < \xi b^{-\eta} \\ 0 & \text{otherwise.} \end{cases} \tag{15}$$

The step by step derivation is methodological and has been omitted due to space constraints. Finally, the interference from a node depends on the amplitude of the received pulse, not its energy. If we define $e_s = \sqrt{e_p}$, the PDF of E_s is now given by

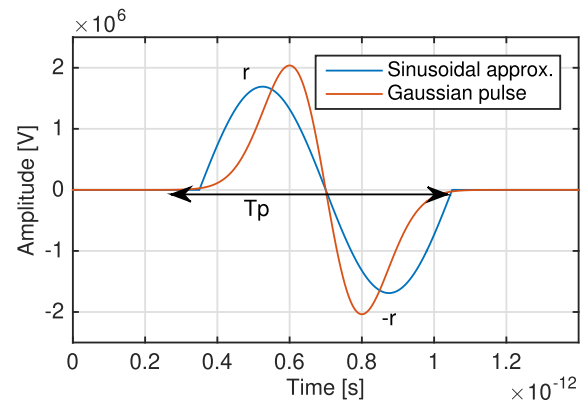

Fig. 4. Sinusoidal approximation of the transmitted pulse in TS-OOK.

$$f_{E_s}(e_s) = \begin{cases} \dfrac{4\xi^{2/\eta} |e_s|^{-\frac{\eta+4}{\eta}}}{(a^2-b^2)\eta} & \text{for } \sqrt{\xi a^{-\eta}} < e_s < \sqrt{\xi b^{-\eta}} \\ 0 & \text{otherwise.} \end{cases} \tag{16}$$

On the other hand, in order to capture the constructive or destructive addition of the interference at the receiver, we need to take into account the shape of the transmitted pulse, which is deterministic, and the time instant at which it reaches the receiver. Since the pulse inter-arrival time is uniformly distributed in T_s, we can first find the PDF of the pulse by modeling time as a random variable T with uniform distribution over the pulse duration T_p,

$$f_T(t) = \begin{cases} \dfrac{1}{T_p} & \text{for } 0 < t < T_p \\ 0 & \text{otherwise.} \end{cases} \tag{17}$$

As before, to obtain the PDF of P, we need to first obtain the inverse function of $p(t)$, which in this case is given by (9). However, this cannot be obtained in closed form expression. To overcome this limitation, we approximate the transmitted pulse with a shifted sinusoidal pulse of same duration T_p, as shown in Figure 4. This pulse can be expressed mathematically as follows

$$p(t) = \begin{cases} r \sin\left(\dfrac{2\pi}{T_p}\left(t - \dfrac{T_p}{2}\right)\right) & \text{for } 0 < t < T_p \\ 0 & \text{otherwise.} \end{cases} \tag{18}$$

where $r = \sqrt{\frac{2}{T_p}}$ is the amplitude of the sinusoid normalized to have unit energy. The inverse function of this new pulse can be written as

$$t = f^{-1}(p) = \frac{T_p}{2\pi} \sin^{-1}\left(\frac{p}{r}\right) + \frac{T_p}{2}. \tag{19}$$

Now the the PDF of P can be derived from the PDF of T similarly as for E_P, yielding to

$$f_P(p) = \begin{cases} \dfrac{1}{\pi r\sqrt{1-\frac{p^2}{r^2}}} & \text{for } -r < p < r \\ 0 & \text{otherwise.} \end{cases} \tag{20}$$

Lets denote the TSOOK symbol as $s(t)$ which can be defined as

$$s(t) = \begin{cases} p(t) & \text{for } 0 < t < T_p \\ 0 & \text{for } T_p < t < T_s. \end{cases} \tag{21}$$

The corresponding random variable S is a mixed one whose discrete and continuous parts can be written as

$$S = \begin{cases} P & \text{with probability } \dfrac{T_p}{T_s} \\ 0 & \text{with probability } \left(1 - \dfrac{T_p}{T_s}\right). \end{cases} \tag{22}$$

where P is the random variable with its value defined in (18). The interference generated by one user over the symbol duration is the product of two random variables E_s and S. Lets define the product random variable as I_u which can be written as

$$I_u = E_s S = \begin{cases} E_s P & \text{with probability } \dfrac{T_p}{T_s} \\ 0 & \text{with probability } \left(1 - \dfrac{T_p}{T_s}\right). \end{cases} \tag{23}$$

Lets define $Y = E_s P$. Therefore the PDF of I_u can be written as

$$f_{I_u}(i_u) = \begin{cases} \dfrac{T_p}{T_s} f_Y(y = i_u) & \text{when } i_u \neq 0 \\ \left(1 - \dfrac{T_p}{T_s}\right) & \text{when } i_u = 0. \end{cases} \tag{24}$$

where $f_Y(y)$ can be determined from the PDFs of E_s and P as (25).

$$f_Y(y) = \begin{cases} \displaystyle\int_{\frac{-y}{r}}^{\sqrt{\xi}b^{-\frac{\eta}{2}}} f_{E_s}(e_s) f_P\left(\frac{y}{e_s}\right)\frac{1}{|e_s|} de_s, \\ \quad -\sqrt{\xi}rb^{-\frac{\eta}{2}} < y < -\sqrt{\xi}ra^{-\frac{\eta}{2}} \\ \displaystyle\int_{\sqrt{\xi}a^{-\frac{\eta}{2}}}^{\sqrt{\xi}b^{-\frac{\eta}{2}}} f_{E_s}(e_s) f_P\left(\frac{y}{e_s}\right)\frac{1}{|e_s|} de_s, \\ \quad -\sqrt{\xi}ra^{-\frac{\eta}{2}} < y < \sqrt{\xi}ra^{-\frac{\eta}{2}} \\ \displaystyle\int_{\frac{y}{r}}^{\sqrt{\xi}b^{-\frac{\eta}{2}}} f_{E_s}(e_s) f_P\left(\frac{y}{e_s}\right)\frac{1}{|e_s|} de_s, \\ \quad \sqrt{\xi}ra^{-\frac{\eta}{2}} < y < \sqrt{\xi}rb^{-\frac{\eta}{2}} \\ 0 \quad \text{otherwise} \end{cases} \tag{25}$$

The derivation of the limits of integration in (25) is given in Appendix A.The integral in (25), when evaluated, yields (26), shown at the bottom of the next page, where ${}_2F_1()$ is the Hyper-geometric function. The final analytical expression for interference from single user can be found by applying the integral limits in (25) to the above expression (26). The detailed derivation of (26) is given in Appendix B. From (26), it can be seen that, the interference from a single user depends on the initial energy ξ, energy decay coefficient η, amplitude of the pulse r, the minimum separation between the receiver and the interferer b and the radius of the interference region a. For example, the higher the initial energy, the wider the interference distribution curve and hence the higher chance of interference level getting higher.

Since the signals from individual nodes add up at the receiver and are independent, the PDF of the total interference can be determined by the convolution of the individual PDFs:

$$f_I(i) = f_{I_1}(i_1) * f_{I_2}(i_2) * f_{I_3}(i_3) * \ldots * f_{I_U}(i_U). \tag{27}$$

To calculate the n-fold convolution on the right hand side, we go into transform domain. We define the characteristic function of the interference from node u as

$$\phi_u(\omega) = E\left[e^{j\omega i_u}\right]. \tag{28}$$

Since the interferences from nodes are independent and identically distributed random variables, they have the same characteristic function. The convolution becomes a product in the transform domain and, thus, the characteristic function of the interference can be written as

$$\phi(\omega) = \left(\phi_u(\omega)\right)^U. \tag{29}$$

Now the PDF of the total interference can be found by taking the inverse transform of $\phi(\omega)$:

$$f_I(i) = F^{-1}\{\phi(\omega)\}. \tag{30}$$

Unfortunately, this characteristic function cannot be analytically derived in closed form, and, thus, we numerically obtain it in the next section. Since the noise is also additive, the PDF of noise plus interference from N users can also be found by convolving their individual PDFs

$$f_{I+N}(i+n) = f_I(i) * f_N(n). \tag{31}$$

where $f_{I+N}(i+n)$ is the PDF of noise plus interference and $f_N(n)$ is the PDF of noise. We note that having a closed-form result for the interference with N users would be beneficial, but if the only way to achieve that is by making assumptions that can compromise the correctness of the model, we would rather refer from doing so.

For modeling the blockage, we use the analysis presented in [12] for circular obstacles. According to the model, the probability that there is no obstacle on the path between the transmitter and receiver depends on the radius of the obstacle r_O, the density of the obstacles λ and separation between the transmitter and the receiver d. This probability is called the line-of-sight (LOS) probability and is given as follows

$$P_{LOS}(d) = e^{-\lambda(2r_O d + \pi r_O^2)}. \tag{32}$$

The effect of the blockage by the obstacles is that some of the multipaths components will be blocked which essentially will decrease the number of convolutions in (27) from U to $\lfloor P_{LOS}(d) \times U \rfloor$.

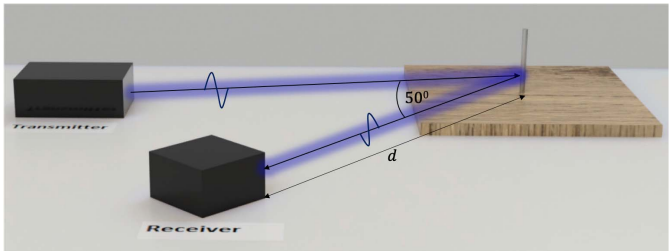

Fig. 5. Illustration of the THz signal strength measurement as a function of distance.

V. Experimental and Numerical Results

A. Experimental Setup

In order to experimentally emulate THz communication signals emanating from multiple THz nodes, we utilize a THz time-domain spectroscopy (THz-TDS) system combined with an innovative interference generating setup. THz-TDS is a non-contact electromagnetic technique analogous to pulsed-ultrasound with the added capability of spectroscopic characterization. The TD-THz sensor emits a near-single cycle electromagnetic pulse with a bandwidth from 0.1 to 3 THz. This extremely wide bandwidth pulse is reflected off of metal rods and pulses are generated from each reflection. No contact is required of the emitter with the metal rod. Using a T-Ray 2000 Spectroscopy system, a terahertz pulse is generated and detected in the time domain where the electric field of the pulse is measured as a function of time. In particular, a collimated 3 cm wide THz-TDS beam is used to illuminate a group of metal rods. The metallic rods are 1 mm in diameter and can effectively reflect the THz pulses. Therefore, each rod effectively represents an interferer at a different distance.

In general, multi-user interference results from uncorrelated signals from different users, otherwise it should be accounted as multi-path propagation. However, the reason why in pulse-based THz communication networks we can artificially generate multi-user interference starting from a single transmitter and a set of reflecting rods is because, whether correlated or uncorrelated, all the signals are composed of either identical pulses or silences, the only difference between the different signals is the delay/time at which they were transmitted and their amplitude or strength. Therefore, for this scheme, multi-path propagation and random multi-user interference are so closely related.

For the first set of measurements, an apparatus was created to hold a metal rod. The THz transmitter is positioned 30 cm away from the rod. The receiver is set at 50 degrees from the transmitter (Fig. 5). Reflected pulse obtained by the receiver shows the presence of a metal rod. Data is collected by taking scans of the reflections from metal rod and obtaining the results in time domain. Fig. 6 shows the THz time domain waveform for the reflection off of the metal rod. The reflected pulse shows that the rod can represent a virtual interfering transmitter.

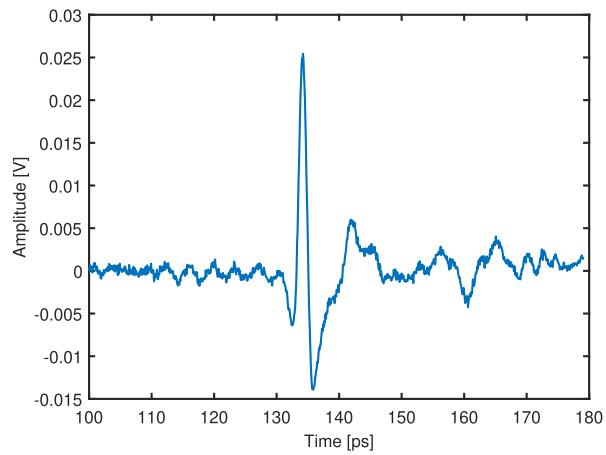

Fig. 6. THz pulse from the reflection off of the metal rod.

In order to validate our hypothesis that a metallic rod in reflection can emulate a THz transmitter, we would first like to note that metals are good reflecting materials at THz frequencies, and, that the diameter of a rod is several wavelengths at THz frequencies. Then, we have utilized COMSOL Multi-physics, a commercial finite-element methods simulation platform, to illustrate the radar cross section and the reflected signals from a metallic rod. We perform a COMSOL time-dependent transient electromagnetic simulation in 2D of the reflected signal from a metal cylinder. A time domain analysis allows us to implicitly validate the system response over the entire frequency range of interest (from 100 GHz to 4 THz in this case). We transmit a 700 femtosecond long Gaussian pulse which have frequency range 0.1-4 THz. An isotropic point dipole located at the left edge of a circular region of radius 8 times the wavelength of the mesh is used as EM source. The circular cylinder is centered at the origin (Fig. 7) and has a radius of 3 times the wavelength. In Fig. 7(a), we show the normalized electrical field at simulation time 1.2121×10^{-12} s for when there is a cylinder at the origin. We show the normalized electric field when there is no cylinder in Fig. 7(b). Finally, we show the difference (i.e., the scattered field) of the previous two fields in Fig. 7(c). From the third figure, we can see that the cylinder can uniformly reflect the signal in a wide range of directions. For verification purpose, we also define several EM point probes at equal distance around the cylinder and observe the reflected pulse at different angles around the circular cylinder. From the figure (Fig. 8), we confirm that the circular cylinder can reflect the signal over a wide range of angles. The delay between the pulses is due to the different distance covered by the pulses to reach the probes at different angles. As a consequence,

$$\int f_{E_s}(e_s)\, f_P\left(\frac{y}{e_s}\right)\frac{1}{|e_s|}de_s = -\frac{4\xi^{2/\eta}|e_s|^{-\frac{\eta+4}{\eta}}\,{}_2F_1\left(\frac{1}{2},\frac{\eta+4}{2\eta};\frac{1}{2}\left(3+\frac{4}{\eta}\right);\frac{y^2}{e_s^2 r^2}\right)}{\pi(\eta+4)r\left(a^2-b^2\right)}, \tag{26}$$

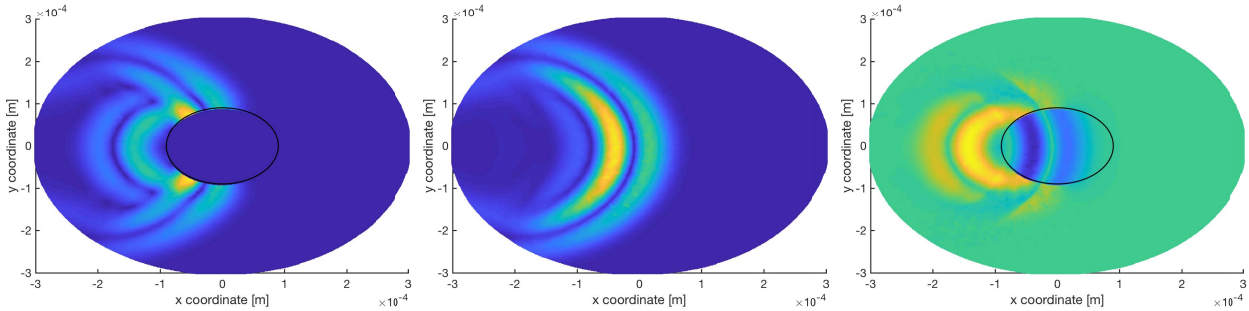

(a) Normalized electric field with cylinder. (b) Normalized electric field without cylinder. (c) Difference field.

Fig. 7. Normalized electric field to show the reflectivity of the cylinder in a wide range of angles.

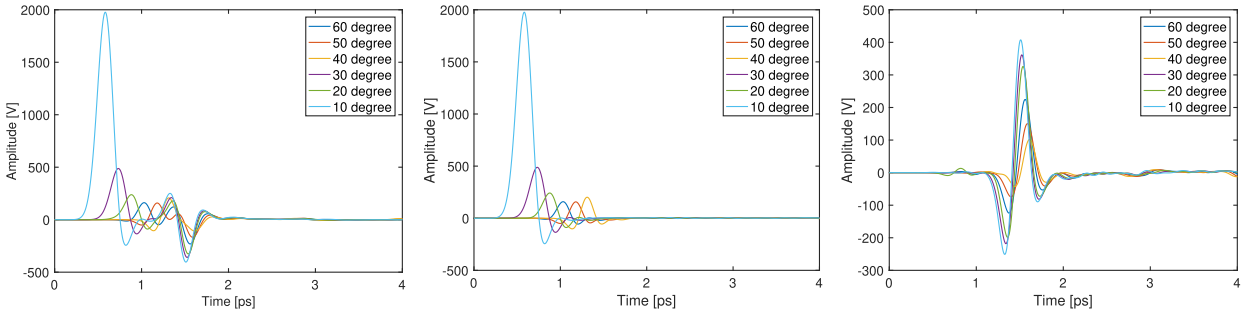

(a) Gaussian pulse with cylinder. (b) Gaussian pulse without cylinder. (c) Reflected Gaussian pulse.

Fig. 8. Normalized electric field to show the reflectivity of the cylinder in a wide range of angles.

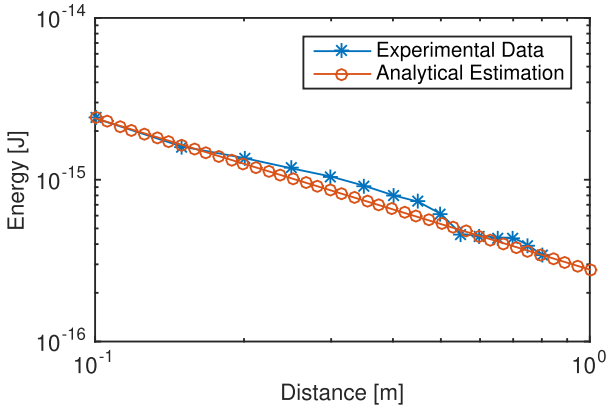

Fig. 9. Measured and approximated received pulse energy as functions of the transmission distance.

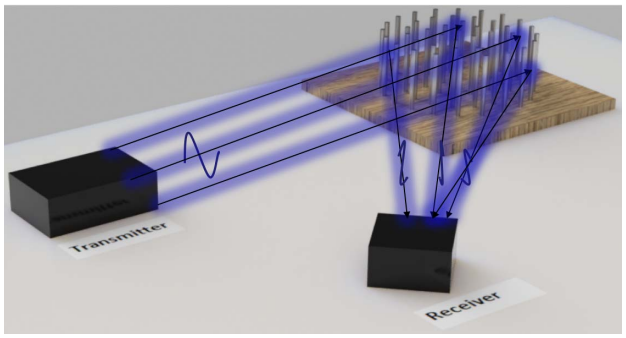

Fig. 10. Illustration of THz beam from the transmitter (Tx) to receiver (Rx) via reflections from the metal rods.

the pulse amplitude decreases as the angle of observation increases.

In Fig. 9, we show the received energy versus distance curve for the measurements taken in the above described setup. The receiver is moved along the line to receive measurements for distances from 10 cm to 1 m. A curve fitting was done to determine the ξ and η values from the experimental data and has been found to be 3.7820e-16 and 0.9357 respectively. The latter confirms the cylindrical spreading of the signal resulting from collimating the emitted THz signals in the experimental setup. These extracted parameter values have then been used in the analytical model to generate the PDF of the interference for different number of nodes in the network. The other parameters of the model have been chosen to match the experimental setup. For example, $T_p = 8$ ps has been approximated from the radiated pulse duration, $\beta = 10$ has been chosen to match the observation period of the measured signal.

To simulate the interference with more realistic and random behavior, we utilize another interference generating setup as shown in Figure 10. A rectangular apparatus (Fig. 11) was used in order to hold multiple metal rods in circular fashion. The apparatus can hold up to 40 rods in place and these 40 positions have been marked with numbers in the figure. The radii of the circle that has positions 21 to 40 is 15 mm. The positions in the center (1-20) vary in distances from the center. Each one was measured individually and their distances from the center are shown in Table 1. The THz transmitter

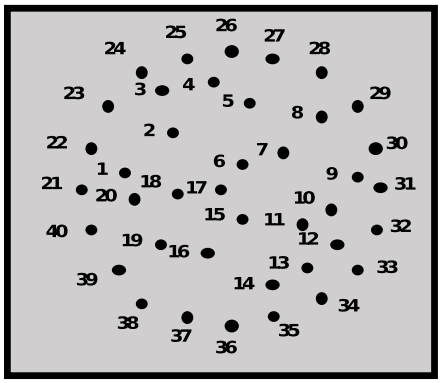

Fig. 11. A zoomed top view of the circular apparatus that holds the metal rods in place.

TABLE I

DISTANCES OF THE POSITIONS ON THE RECTANGULAR APPARATUS FROM THE CENTER OF THE APPARATUS

Position	Distance(mm)	Position	Distance(mm)
1	11	11	6
2	7	12	12
3	12	13	10
4	11	14	13
5	9	15	5
6	3	16	10
7	8	17	2
8	12	18	6
9	13	19	9
10	10	20	11

is positioned so that the THz beam is centered at position 26, 27.5 cm away. The receiver is set at 50 degrees from the transmitter at a distance of 14.5 cm away from a metal rod in position 26. Data was collected by putting 20 rods randomly in the 40 positions and taking scans in the time domain. Fig. 12 shows the THz time domain waveform for the reflections off of 20 metal rods in one distribution. From the figure, we can see that the amplitude of the received pulses is higher in this case. This can be explained by the reflected THz pulses from multiple metal rods reaching the receiver at the same time, causing their pulses to overlap and the amplitude to add up. The reason for time separation among different pulses can be explained as the different path distance traveled by individual reflected pulse.Also, $a = 18.89$ cm and $b = 14.5$ cm was derived from experimental setup as the maximum and minimum distances of the interferers.

Although the distribution of the rods on the plate does not look Poisson, we try to mimic a Poisson distribution by placing the 20 rods among 40 locations and by turning the plate around its center. Then we take measurements for different realizations and combine the data.

B. Model Validation

For the validation of our analytical model, we first determine the distribution of noise by curve fitting to experimental data. Fig. 13 shows the experimental noise distribution along with fitted curve. The mean and standard deviation of the noise distribution were found to be $\mu = -0.0007$V and $\sigma =$

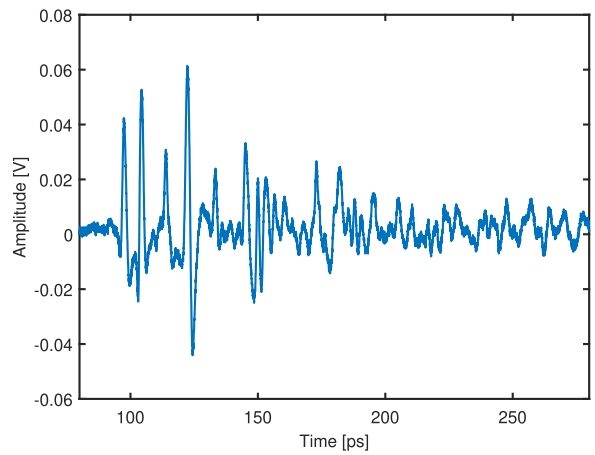

Fig. 12. THz pulse from the reflection off of 20 metal rods distributed in rectangular apparatus.

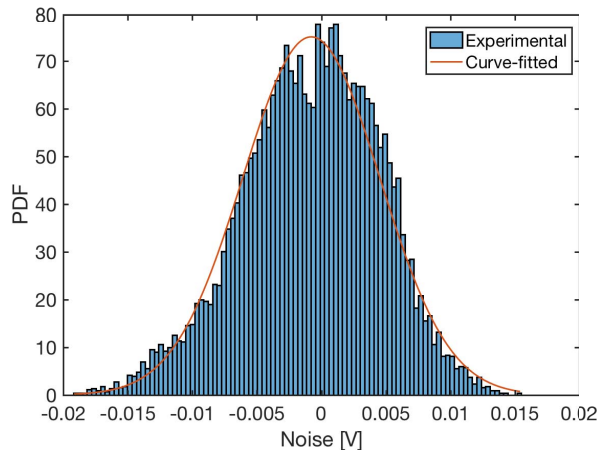

Fig. 13. Noise distribution of the THz-TDS receiver.

0.0053V, respectively. After that, we determine the line of sight probability by considering the wires as obstacles. Considering the arrangement of the wires, the pulse can travel through the obstacles on average a distance equal to the radius of the outer circle (15mm). This gives a LOS probability is of 0.4 which means on average only 8 out 20 reflected rays reach the receiver.

We show the probability distribution function of the interference for both experimental and analytical cases when there are 20 interferers in the network in Fig. 14. Our analytical interference model matches the experimental data very well. The reason for a slight difference in the distribution is that we approximated the THz-TDS pulse with a sinusoidal pulse, but in reality it is not symmetrical above and below the zero line, as shown in fig. 6. As a result, the measured interference PDF is biased towards positive values of interference. In addition, the interferers locations also are not exactly Poisson distributed in the experimental setup as one needs many realizations of the experiments to obtain the satatistical behaviors.

In addition, we were not able to put the receiver at the center of the circular distribution of nodes due to the bigger size of the THz-TDS device. Nevertheless, the distribution

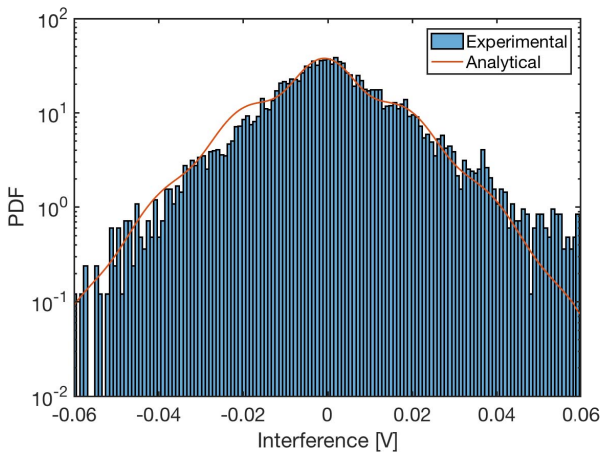

Fig. 14. Interference distribution of 20 interferers with noise added.

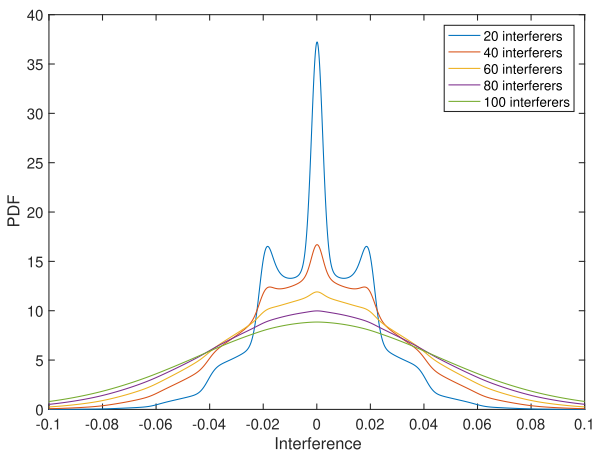

Fig. 15. Illustration of PDF converging to Gaussian with increasing number of nodes.

from the analytical model and experimental data matches very well. It can reasonably be said that, as the number of measurements is increased and the distances are picked randomly, the experimental PDF will more closely follow the analytical model.

Fig. 15 compares the interference PDFs for different number of interferers in the network. It can be seen that the PDF is not Gaussian for number of nodes not much bigger than β. As the number of nodes in the network increases to much greater than β, the interference value spreads away from the 0V and the probability of interference value getting higher increases. For large number of interferers, the PDF converges to a Gaussian PDF as expected from the Central Limit theorem, and originally shown for TS-OOK in [17]. The mean and variance of the total interference can be easily found from the distribution function and used in system level simulation. As an example, the mean and variance of the noise plus interference for the 100 interferers are found to be -0.00078 V and $0.00215\ V^2$ respectively.

VI. Conclusion

In this paper, we have presented an stochastic model for interference in short range pulse-based THz-band communication network. The model considers the fact that interference occurs with the amplitude of the signal, not the power. The PDF of the interference has been analytically deduced from the PDFs of the energy and the pulse shape. On the way, we have utilized the fact that the received energy can be expressed as a polynomial function of distance which we verified from the experimental data as well. In addition, the analytical model has been compared with experimental data to validate the model. The results show good match in spite of the limitation we had in the experimental set up. It has also been shown that the PDF is not Gaussian for few nodes, but converges to a Gaussian distribution as the number of nodes increases in the network. Starting from the interference distribution, the achievable data rate of the pulse based short range THz band communication can be computed which we leave for future work.

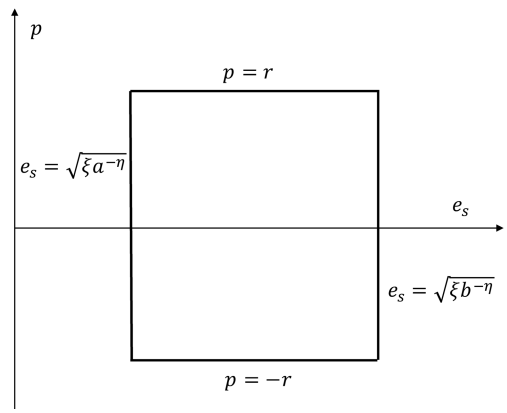

Fig. 16. The boundaries of set A.

Appendix A
Derivation of the Limits of Integration

In deriving the limits of integration, we follow a similar approach shown in [11]. Lets recall the pdfs of the two random varibles here for clarity.

$$f_{E_s}(e_s) = \begin{cases} \dfrac{4\xi^{2/\eta}\,|e_s|^{-\frac{\eta+4}{\eta}}}{(a^2-b^2)\eta} & \text{for } \sqrt{\xi a^{-\eta}} < e_s < \sqrt{\xi b^{-\eta}} \\ 0 & \text{otherwise.} \end{cases} \tag{33}$$

$$f_P(p) = \begin{cases} \dfrac{1}{\pi r\sqrt{1-\frac{p^2}{r^2}}} & \text{for } -r < p < r \\ 0 & \text{otherwise.} \end{cases} \tag{34}$$

Lets define the set $A = \left\{(e_s, p) \mid \sqrt{\xi a^{-\eta}} < e_s < \sqrt{\xi b^{-\eta}}, -r < p < r\right\}$ as depicted in Figure 16. To determine the pdf of the product of E_s and P, lets define an auxiliary variable $y_1 = e_s$ with $y_2 = e_s p$. The joint pdf of y_1 and y_2 is given by the well known result,

$$g(y_1, y_2) = \begin{cases} f_{E_s}(y_1)\, f_P\left(\dfrac{y_2}{y_1}\right)|J|, & (y_1, y_2) \in B \\ 0 & \text{otherwise.} \end{cases} \tag{35}$$

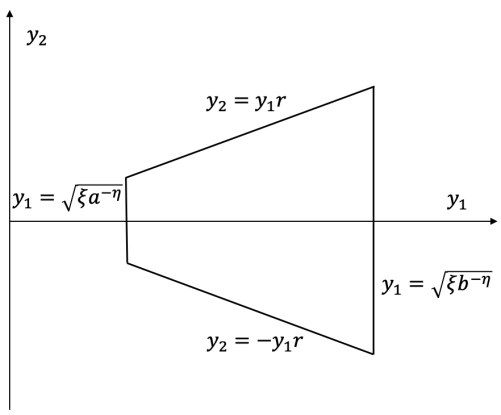

Fig. 17. The boundaries of set B.

where J is the Jacobian of transformation. To find the Jacobian, we first need to find the inverse functions $e_s = y_1$ and $p = \frac{y_2}{y_1}$. Hence, the Jacobian is

$$J = \begin{vmatrix} \dfrac{\partial e_s}{\partial y_1} & \dfrac{\partial e_s}{\partial y_2} \\ \dfrac{\partial p}{\partial y_1} & \dfrac{\partial p}{\partial y_2} \end{vmatrix} = \frac{1}{y_1}. \tag{36}$$

Lets define the mapping of A in the $y_1 y_2$-plane as $B = \left\{(y_1, y_2) \mid \sqrt{\xi a^{-\eta}} < y_1 < \sqrt{\xi b^{-\eta}}, -r y_1 < y_2 < r y_1\right\}$. The boundaries of A are transformed into the boundaries of B as follows

$$\begin{aligned} e_s &= \sqrt{\xi a^{-\eta}} \text{ into } y_1 = \sqrt{\xi a^{-\eta}} \\ e_s &= \sqrt{\xi b^{-\eta}} \text{ into } y_1 = \sqrt{\xi b^{-\eta}} \\ p &= r \text{ into } y_2 = y_1 r \\ p &= -r \text{ into } y_2 = -y_1 r \end{aligned} \tag{37}$$

Accordingly B is shown in Figure 17. Now the limits of integration can be determined from Figure 17 and marginal pdf of y_2 is found as following

$$f_{Y_2}(y_2) = \begin{cases} \displaystyle\int_{-\frac{y_2}{r}}^{\sqrt{\xi b^{-\eta}}} g(y_1, y_2) dy_1 & \text{for } -\sqrt{\xi b^{-\eta}} r < y_2 < -\sqrt{\xi a^{-\eta}} r \\ \displaystyle\int_{\sqrt{\xi a^{-\eta}}}^{\sqrt{\xi b^{-\eta}}} g(y_1, y_2) dy_1 & \text{for } -\sqrt{\xi a^{-\eta}} r < y_2 < \sqrt{\xi a^{-\eta}} r \\ \displaystyle\int_{\frac{y_2}{r}}^{\sqrt{\xi b^{-\eta}}} g(y_1, y_2) dy_1 & \text{for } \sqrt{\xi a^{-\eta}} r < y_2 < \sqrt{\xi b^{-\eta}} r \\ 0 & \text{otherwise.} \end{cases} \tag{38}$$

(25) then can be obtained by simply replacing y_2 with y and y_1 with e_s in the above equation (38).

Appendix B
Derivation of the Indefinite Integral

$$\begin{aligned} &\int f_{E_s}(e_s) f_P\left(\frac{y}{e_s}\right) \frac{1}{|e_s|} de_s \\ &= \int \frac{1}{\pi r \sqrt{1 - \frac{y^2}{e_s^2 r^2}}} \frac{4\xi^{\frac{2}{\eta}} |e_s|^{-\frac{\eta+4}{\eta}}}{(a^2 - b^2)\eta} \frac{1}{|e_s|} de_s \\ &= \frac{4\xi^{\frac{2}{\eta}}}{\pi r (a^2 - b^2)\eta} \int |e_s|^{-1-\frac{\eta+4}{\eta}} \left(1 - \frac{y^2}{e_s^2 r^2}\right)^{-\frac{1}{2}} de_s \\ &= \frac{4\xi^{\frac{2}{\eta}}}{\pi r (a^2 - b^2)\eta} \int_0^{e_s} |t|^{-1-\frac{\eta+4}{\eta}} \left(1 - \frac{y^2}{t^2 r^2}\right)^{-\frac{1}{2}} dt \end{aligned} \tag{39}$$

Substituting $u = \frac{y^2}{t^2\ r^2}$ in the above integral yields,

$$\begin{aligned} &\int_0^{e_s} |t|^{-1-\frac{\eta+4}{\eta}} \left(1 - \frac{y^2}{t^2 r^2}\right)^{-\frac{1}{2}} dt \\ &= -\frac{1}{2} \int_0^{\frac{y^2}{e_s^2 r^2}} \left| \frac{y u^{-\frac{1}{2}}}{r} \right|^{-1-\frac{\eta+4}{\eta}} (1-u)^{-\frac{1}{2}} \left|\frac{y}{r}\right| u^{-\frac{1}{2}-1} du \end{aligned} \tag{40}$$

Substituting $v = \frac{e_s^2\ r^2\ u}{y^2}$ in the above integral yields,

$$\begin{aligned} &-\frac{1}{2} \int_0^1 \left| \frac{y \left(\frac{v y^2}{r^2 e_s^2}\right)^{-\frac{1}{2}}}{r} \right|^{-1-\frac{\eta+4}{\eta}} \left(1 - \frac{v y^2}{r^2 e_s^2}\right)^{-\frac{1}{2}} \left|\frac{y}{r}\right| \\ &\quad \times \left(\frac{v y^2}{r^2 e_s^2}\right)^{-\frac{1}{2}-1} \frac{y^2 e_s^{-2}}{r^2} dv \\ &= -\frac{1}{2} \int_0^1 |e_s|^{-1-\frac{\eta+4}{\eta}} v^{\frac{1}{2}+\frac{\eta+4}{2\eta}} \\ &\quad \times \left(1 - \frac{v y^2}{r^2 e_s^2}\right)^{-\frac{1}{2}} \left|\frac{y}{r}\right| v^{-\frac{1}{2}-1} |e_s|\, e_s^2 \left|\frac{r}{y}\right| \left(\frac{y}{r}\right)^{-2} \frac{y^2 e_s^{-2}}{r^2} dv \\ &= -|e_s|^{-\frac{\eta+4}{\eta}} \frac{1}{2} \int_0^1 v^{\frac{\eta+4}{2\eta}-1} \left(1 - \frac{v y^2}{r^2 e_s^2}\right)^{-\frac{1}{2}} dv \end{aligned} \tag{41}$$

Defining $b = \frac{\eta+4}{2\eta}, c = 1 + \frac{\eta+4}{2\eta}, a\ = \frac{1}{2}$ and $z = \frac{y^2}{r^2\ e_s^2}$ in the definition of Hyper-geometric function, the above integral can be written as

$$= -|e_s|^{-\frac{\eta+4}{\eta}} \frac{\eta}{\eta+4}\, {}_2F_1\left(\frac{1}{2}, \frac{\eta+4}{2\eta}; \frac{1}{2}\left(3 + \frac{4}{\eta}\right); \frac{y^2}{e_s^2 r^2}\right) \tag{42}$$

Replacing the value of the above integral in (39) yields,

$$\begin{aligned} &= \frac{4\xi^{\frac{2}{\eta}}}{\pi r (a^2 - b^2)\eta} \\ &\quad \times -|e_s|^{-\frac{\eta+4}{\eta}} \frac{\eta}{\eta+4}\, {}_2F_1\left(\frac{1}{2}, \frac{\eta+4}{2\eta}; \frac{1}{2}\left(3 + \frac{4}{\eta}\right); \frac{y^2}{e_s^2 r^2}\right) \\ &= -\frac{4\xi^{\frac{2}{\eta}} |e_s|^{-\frac{\eta+4}{\eta}}}{\pi (\eta+4) r (a^2 - b^2)}\, {}_2F_1\left(\frac{1}{2}, \frac{\eta+4}{2\eta}; \frac{1}{2}\left(3 + \frac{4}{\eta}\right); \frac{y^2}{e_s^2 r^2}\right) \end{aligned} \tag{43}$$

REFERENCES

[1] I. F. Akyildiz, J. M. Jornet, and C. Han, "Terahertz band: Next frontier for wireless communications," *Phys. Commun.*, vol. 12, p. 16–32, Sep. 2014.

[2] J. G. Andrews, R. K. Ganti, M. Haenggi, N. Jindal, and S. Weber, "A primer on spatial modeling and analysis in wireless networks," *IEEE Commun. Mag.*, vol. 48, no. 11, pp. 156–163, Nov. 2010.

[3] P. Cardieri, "Modeling interference in wireless ad hoc networks," *IEEE Commun. Surveys Tuts.*, vol. 12, no. 4, pp. 551–572, 4th Quart., 2010.

[4] S. Cherry, "Edholm's law of bandwidth," *IEEE Spectr.*, vol. 41, no. 7, pp. 58–60, Jul. 2004.

[5] H. ElSawy, A. Sultan-Salem, M. S. Alouini, and M. Z. Win, "Modeling and analysis of cellular networks using stochastic geometry: A tutorial," *IEEE Commun. Surveys Tuts.*, vol. 19, no. 1, pp. 167–203, 1st Quart., 2017.

[6] J. Federici and L. Moeller, "Review of terahertz and subterahertz wireless communications," *J. Appl. Phys.*, vol. 107, no. 11, 2010, Art. no. 111101.

[7] J. Federici, L. Moeller, and K. Su, *Terahertz Communication*. Belvidere, IL, USA: Woodhead, 2013.

[8] A. C. Ferrari *et al.*, "Science and technology roadmap for graphene, related two-dimensional crystals, and hybrid systems," *Nanoscale*, vol. 7, no. 11, pp. 4598–4810, 2015.

[9] M. Gapeyenko *et al.*, "Analysis of human-body blockage in urban millimeter-wave cellular communications," in *Proc. IEEE Int. Conf. Commun. (ICC)*, May 2016, pp. 1–7.

[10] M. Haenggi and R. K. Ganti, "Interference in large wireless networks," *Found. Trends Netw.*, vol. 3, no. 2, pp. 127–248, 2009.

[11] R. V. Hogg, J. McKean, and A. T. Craig, *Introduction to Mathematical Statistics*. Upper Saddle River, NJ, USA: Prentice-Hall, 1995.

[12] Z. Hossain, C. Mollica, and J. M. Jornet, "Stochastic multipath channel modeling and power delay profile analysis for terahertz-band communication," in *Proc. 4th ACM Int. Conf. Nanosc. Comput. Commun.*, 2017, Art. no. 32.

[13] Z. Hossain, S. H. Vedant, C. R. Nicoletti, and J. F. Federici, "Multi-user interference modeling and experimental characterization for pulse-based terahertz communication," in *Proc. 3rd ACM Int. Conf. Nanosc. Comput. Commun.*, 2016, Art. no. 3.

[14] J. M. Jornet, "Low-weight error-prevention codes for electromagnetic nanonetworks in the terahertz band," *Nano Commun. Netw.*, vol. 5, nos. 1–2, pp. 35–44, Mar./Jun. 2014.

[15] J. M. Jornet and I. F. Akyildiz, "Channel modeling and capacity analysis for electromagnetic wireless nanonetworks in the terahertz band," *IEEE Trans. Wireless Commun.*, vol. 10, no. 10, pp. 3211–3221, Oct. 2011.

[16] J. M. Jornet and I. F. Akyildiz, "Graphene-based plasmonic nano-antenna for terahertz band communication in nanonetworks," *IEEE J. Sel. Areas Commun.*, vol. 31, no. 12, pp. 685–694, Dec. 2013.

[17] J. M. Jornet and I. F. Akyildiz, "Femtosecond-long pulse-based modulation for terahertz band communication in nanonetworks," *IEEE Trans. Commun.*, vol. 62, no. 5, pp. 1742–1754, May 2014.

[18] J. M. Jornet and I. F. Akyildiz, "Graphene-based plasmonic nano-transceiver for terahertz band communication," in *Proc. 8th Eur. Conf. Antennas Propag. (EuCAP)*, Apr. 2014, pp. 492–496.

[19] J. Kokkoniemi, J. Lehtomäki, and M. Juntti, "Stochastic geometry analysis for mean interference power and outage probability in THz networks," *IEEE Trans. Wireless Commun.*, vol. 16, no. 5, pp. 3017–3028, May 2017.

[20] Y. Kurita *et al.*, "Ultrahigh sensitive sub-terahertz detection by inp-based asymmetric dual-grating-gate high-electron-mobility transistors and their broadband characteristics," *Appl. Phys. Lett.*, vol. 104, no. 25, 2014, Art. no. 251114.

[21] T. Kürner and S. Priebe, "Towards THz communications-status in research, standardization and regulation," *J. Infr., Millim., THz. Waves*, vol. 35, no. 1, pp. 53–62, Jan. 2014.

[22] Q. Y. Lu, S. Slivken, N. Bandyopadhyay, Y. Bai, and M. Razeghi, "Widely tunable room temperature semiconductor terahertz source," *Appl. Phys. Lett.*, vol. 105, no. 20, 2014, Art. no. 201102.

[23] Q. Lu, D. Wu, S. Sengupta, S. Slivken, and M. Razeghi, "Room temperature continuous wave, monolithic tunable THz sources based on highly efficient mid-infrared quantum cascade lasers," *Sci. Rep.*, vol. 6, Mar. 2016, Art. no. 23595.

[24] K. S. Novoselov, V. I. Fal'ko, L. Colombo, P. R. Gellert, M. G. Schwab, and K. Kim, "A roadmap for graphene," *Nature*, vol. 490, no. 7419, pp. 192–200, 2012.

[25] I. Oppermann, M. Hämäläinen, and J. Iinatti, *UWB: Theory and Applications*. Hoboken, NJ, USA: Wiley, 2005.

[26] V. Petrov, M. Komarov, D. Moltchanov, J. M. Jornet, and Y. Koucheryavy, "Interference and SINR in millimeter wave and terahertz communication systems with blocking and directional antennas," *IEEE Trans. Wireless Commun.*, vol. 16, no. 3, pp. 1791–1808, Mar. 2017.

[27] V. Petrov, D. Moltchanov, and Y. Koucheryavy, "Interference and SINR in dense terahertz networks," in *Proc. IEEE 82nd Veh. Technol. Conf. (VTC-Fall)*, Sep. 2015, pp. 1–5.

[28] S. Priebe and T. Kurner, "Stochastic modeling of THz indoor radio channels," *IEEE Trans. Wireless Commun.*, vol. 12, no. 9, pp. 4445–4455, 2013.

[29] V. Radisic *et al.*, "Sub-millimeter wave InP technologies and integration techniques," in *IEEE MTT-S Int. Microw. Symp. Dig.*, May 2015, pp. 1–4.

[30] S. Slivken and M. Razeghi, "High power, electrically tunable quantum cascade lasers," *Proc. SPIE*, vol. 9755, Feb. 2016, Art. no. 97550C.

[31] K. Venugopal, M. C. Valenti, and R. W. Heath, Jr., "Interference in finite-sized highly dense millimeter wave networks," in *Proc. Inf. Theory Appl. Workshop (ITA)*, Feb. 2015, pp. 175–180.

[32] K. Venugopal, M. C. Valenti, and R. W. Heath, Jr., "Device-to-device millimeter wave communications: Interference, coverage, rate, and finite topologies," *IEEE Trans. Wireless Commun.*, vol. 15, no. 9, pp. 6175–6188, Sep. 2016.

[33] B. S. Williams, "Terahertz quantum-cascade lasers," *Nature Photon.*, vol. 1, no. 9, pp. 517–525, 2007.

[34] M. Z. Win, P. C. Pinto, and L. A. Shepp, "A mathematical theory of network interference and its applications," *Proc. IEEE*, vol. 97, no. 2, pp. 205–230, Feb. 2009.

[35] X.-W. Yao, C.-C. Wang, W.-L. Wang, and C. Han, "Stochastic geometry analysis of interference and coverage in terahertz networks," *Nano Commun. Netw.*, vol. 13, pp. 9–19, Sep. 2017.

Zahed Hossain received the B.S. degree in electronic and telecommunication engineering from North South University, Bangladesh, in 2010, and the M.S. and Ph.D. degrees in electrical engineering from the University at Buffalo, The State University of New York (UB), in 2014 and 2018, respectively. This work was completed at the University at Buffalo, as part of his Ph.D. work under the supervision of Prof. J. M. Jornet. From 2010 to 2012, he was a Lab Instructor with North South University. He was a Lecturer with North South University and taught Signals and Systems in the summer from 2014 to 2017. He is currently a Wireless Standards Systems Engineer with Intel Corporation. His current research interests include modulation, channel modeling, multi-user interference modeling, protocol design, performance analysis and network simulation for Terahertz-band communication networks, with applications in terabit wireless personal and local area networks, next generation small cells, wireless nanosensor networks, and the Internet of Nano-Things. He was a recipient of the Best Paper Award for ACM NanoCom in 2017.

Carley N. Mollica received the B.Sc. degree in physics and the B.Sc. degree in mathematics from Wagner College, Staten Island, NY, USA. She is currently pursuing the Ph.D. degree in materials science and engineering the New Jersey Institute of Technology under the supervision of Dr. J. Federici. She was supported there in her first four years by the Provost Gary Thomas Doctoral Fellowship Program. Prior to attending graduate school, she participated in a Physics REU Program at the University of Florida. While there, she worked on micro-electro-mechanical system (MEMS) pressure sensors testing at 4.2 K to measure their pressure sensitivity, to evaluate their suitability for the detection of quantum turbulence. Her current research interests include non-destructive evaluation of materials using an electromagnetic technique, specifically involved in terahertz time domain spectroscopy to accurately assess the durability of paints.

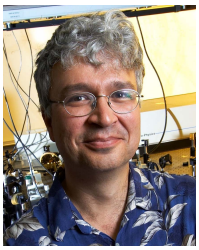

John F. Federici received the B.S. degree in physics from the University of Notre Dame in 1983 and the Ph.D. degree in plasma physics from Princeton University in 1989. After a post-doctoral appointment at Bell Laboratories, he joined the Physics Department Faculty, New Jersey Institute of Technology. He is currently a Distinguished Professor with the Department of Physics, New Jersey Institute of Technology. He has been the lead writer on more than 70 publications in scholarly journals and holds seven patents. In 2005, he received NJIT's Top Research Honor, the Harlan Perlis Research Award, and in 2005 accepted an award for his Terahertz work from the Research and Development Council of New Jersey. Since his days at Bell Laboratories, he has been active in THz spectroscopy, imaging, and most recently THz wireless communications research.

Josep Miquel Jornet received the B.S. degree in telecommunication engineering and the M.Sc. degree in information and communication technologies from the Universitat Politecnica de Catalunya, Barcelona, Spain, in 2008, and the Ph.D. degree in electrical and computer engineering from the Georgia Institute of Technology (Georgia Tech), Atlanta, GA, USA, in 2013. From 2007 to 2008, he was a Visiting Researcher with the Massachusetts Institute of Technology (MIT), Cambridge. He is currently an Associate Professor with the Department of Electrical Engineering, University at Buffalo, The State University of New York. He is serving as the lead PI on multiple grants from U.S. federal agencies including the National Science Foundation, the Air Force Office of Scientific Research and the Air Force Research Laboratory. His current research interests are in terahertz-band communication networks, nanophotonic wireless communication, wireless nano-bio-sensing networks and the Internet of Nano-Things. In these areas, he has coauthored more than 100 peer-reviewed scientific publications, 1 book, and has also been granted three U.S. patents. He was a recipient of the National Science Foundation CAREER Award and of several other awards from IEEE, ACM, and UB. Since 2016, he has been the Editor-in-Chief of the *Nano Communication Networks* (Elsevier) Journal.